NANO LETTERS

2007
Vol. 7, No. 11
3399−3404

Integration of Individual Nanoscale Structures into Devices Using Dynamic Nanostenciling

Stefan Egger,*,† Adelina Ilie,‡,§ Shinichi Machida,|| and Tomonobu Nakayama||

International Center for Young Scientists, National Institute for Materials Science, 1-1 Namiki, Tsukuba, Ibaraki 305-0044, Japan, Department of Physics, University of Bath, Bath BA2 7AY, United Kingdom, Nanoscience, University of Cambridge, 11 J. J. Thomson Avenue, Cambridge CB3 0FF, United Kingdom, and Nano System Functionality Center, National Institute for Materials Science, 1-1, Namiki, Tsukuba, Ibaraki 305-0044, Japan

Received July 22, 2007; Revised Manuscript Received September 18, 2007

ABSTRACT

We succeeded in integrating individual, pre-existing nanostructures into functional devices using ultrahigh vacuum dynamic nanostenciling and show working devices based on single-walled carbon nanotubes, a benchmark nanomaterial, and porphyrin J-aggregates, a "soft" supramolecular nanomaterial. Nanostructures are first located via atomic force microscopy, while device elements are added step by step, with an achieved positional accuracy of 20 nm, using a shadow mask assembly that moves while being exposed to evaporated material. Electronic transport, potentiometry, and scanning Kelvin probe were used for control at any fabrication stage and were available in situ. Such complex fabrication/characterization capabilities, applicable repeatedly, reliably, and nondestructively, pave the way for dynamic nanostenciling instrumentation to establish itself as a viable tool for easy integration and prototyping of fragile nanostructures synthesized through a wide range of processes.

In recent years, there has been an explosion in synthesizing new nanomaterials through a large variety of methods. Many of these materials can be classed as fragile, either because they are composed of a limited number of atomic layers[1] or rows[2,3] (in 2D or 1D, respectively) or because they are "soft", i.e., of biological or molecular nature.[4] There are also various hybrids of inorganic and soft materials.[5] Because of this fragile nature, they face an unsolved problem, which is how to integrate them at an individual level into devices without altering their structure and, consequently, their properties during device fabrication. Some nanofabrication techniques are being promoted as suitable for integration of nanostructures, the most successful ones being based on electron or focused ion beams.[6−9] These are able to locate by beam scanning a specific, individual nanostructure before patterning contacts on it using various beam-assisted processes. However, their main drawback is that, because they rely on charged particles of energies in the order of keV, they can damage sensitive structures[7] and induce contamination and changes in the substrate over an extended area[8] that can alter the properties of the resulting devices.

A nondestructive alternative is first to fabricate inert electrodes, ideally coplanar with the substrate,[10] and then position the nanostructures on top of them. However, the current injection point is now undefined[11] and the nanostructure is deformed if the electrodes are noncoplanar,[12] while the choice of geometry and materials for the electrodes is very limited. Moreover, such an approach is not ideal for integrating individual nanostructures.

For fragile nanostructures, we need a nanofabrication technique that is nondestructive by its very nature,[13] with the general requirement that electrodes are formed on top of an individual structure. By its promise, dynamic nanostenciling appears to be ideally suited for this purpose. This technique uses a stencil mask that is moved over a surface with nanometer precision, using piezo-actuation, while "drawing" nanopatterns of materials sourced by gentle thermal evaporation.[14−16] A pre-existing, specific nanostructure, or even parts of it, could in principle thus be located and device integrated without any modification to its structure.

Here we show for the first time that real, individual nanostructures can be integrated into functional devices using

* Corresponding author. E-mail: stefan.egger@alumni.ethz.ch.
† International Center for Young Scientists, National Institute for Materials Science.
‡ Department of Physics, University of Bath.
§ Nanoscience, University of Cambridge.
|| Nano System Functionality Center, National Institute for Materials Science.

10.1021/nl071778m CCC: $37.00
Published on Web 10/09/2007

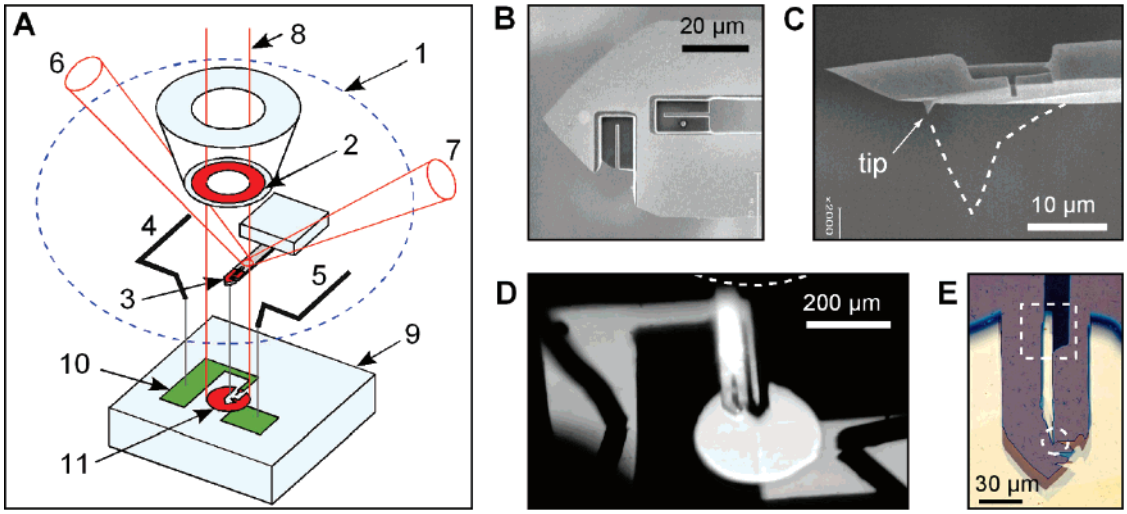

Figure 1. Key parts of the mask-cantilever-probe assembly and its functions. (A) The assembly (1) is aligned relative to the large scale pad structure (10), fabricated on the substrate (9) in a previous step using an additional large-scale mask. The molecular beam (8) from the e-beam evaporator passes successively through the collimation mask (2) and the cantilever-mask (3) and condenses on a small circular area (11) on the substrate. The collimation mask (2) defines the pattern (11) in such a way that this only contacts one of the large pads of the structure (10) and avoids large-area coating that would short-circuit the whole device. The cantilever-mask (3) defines the nanoelectrodes. The laser beam used for detection of cantilever deflection in AFM mode is focused on the shaft of the cantilever behind the collimated molecular beam and follows the optical path (6,7). The two probes (4,5) used for electrical characterization touch the large-scale pads after the cantilever (3) has approached the surface in noncontact AFM mode. (B) Top and (C) side views of the modified commercial AFM cantilever. FIB is used to cut apertures and to shorten the tip. The dashed line indicates the original tip profile. (D) Image of sample, cantilever, electrical probes, and collimator (dashed line), recorded through a view port under an angle of 45°. The sample was moved 60 μm side ways relative to the fabrication position. (E) Ex situ optical image of electrode structures. The location of the nanodevice and the connection to the large-scale pad structure are marked with a circle and a square, respectively.

dynamic nanostenciling. As examples, we used single-walled carbon nanotubes (SWCNTs) and porphyrin J-aggregates formed by supramolecular assembly.[17,18] Both types of nanostructures are one-dimensional, with lateral sizes from one to a few nanometers, while the length of them probed by the nanofabricated contacts could be made as small as 20 nm. Carbon nanotubes were chosen as a benchmark due to their well-known electrical behavior, while porphyrin J-aggregates are a new example of a soft, fragile organic structure that would be destroyed by exposure to beams or lithographic procedures. To demonstrate the functionality of the devices produced, we used advanced in situ characterization. For this, we extended the range of in situ characterizations already integrated with the nanofabrication capability[19] so that the devices could be tested using in situ three-terminal transport measurements, Kelvin-probe microscopy, and potentiometry.

The ultrahigh vacuum (UHV) nanostencil instrument has the same basic setup as described previously.[19,20] Several unique features of dynamic nanostenciling have been exhaustively demonstrated by ourselves and others. They involved almost exclusively structures and devices that were produced entirely with the stencil. Such demonstrations used the technique's capabilities to move freely, allowing one to obtain free shapes[16] and variable thickness,[20] to precisely overlap structures,[14,19,21] to combine materials easily,[20,22] e.g., for combinatorial chemistry applications,[19] to use materials that cannot be patterned with other techniques,[23] and to fabricate in situ full devices, from nano to micro level.[19,20] Thus, there is an unsurpassed flexibility in combining shapes and materials.

However, to construct a device around a chosen, preexisting nanostructure, i.e., which was not produced with the stencil, is much harder, as it requires the nanostencil successfully combining three requirements: (i) to scan in atomic force microscopy (AFM) mode to locate the nanostructure with the same cantilever that will be used subsequently for nanofabrication, (ii) to fabricate contacts and functional elements on/around the found structure with nanometer precision, while, at the same time, (iii) to be able to mask appropriately the fabricated structures in order to avoid shortcircuits. So far, the most advanced attempt to connect nanostructures[24] did not produce an electrically measurable device, while the demonstration structures where connection was attempted were "artificial", i.e., made with the stencil, and tens of nm wide.

The technical novelty crucial for enabling the success of this work was the development of a special mask-cantilever-probe assembly, (1) in Figure 1A. This is meant to define the nanoscale parts of the interconnects while fulfilling the requirements outlined above. All its three key elements, collimation mask (2), mask-cantilever (3), and electrical probes (4,5), pictured inside the circled area in Figure 1A, are mounted on the *same* base. The procedure for their relative alignment is detailed below. Overall, the compactness of this design considerably simplifies the setup and operation of the instrument. The sighting of the cantilever/sample is free, as shown in Figure 1D, allowing easy coarse navigation and laser alignment. The ease of this approach was proved ultimately to be the key in enabling successful interconnection of real, arbitrary nanostructures. This contrasts with the difficulty in usage and performance of other existing designs

based on *separate* (moveable or fixed-installation) components,[19,24] which require multiple, successive relative alignments leading to accumulated errors in pattern positioning.

The mask-cantilever (3) has the dual role of defining the nanoscale electrical contacts during nanofabrication and is also used for scanning while performing nanostructure location or AFM-based characterization.[16,24−26] It is obtained by modifying a commercial cantilever using focused ion beam (FIB) as in Figure 1B,C, with thinned micrometer-sized areas in which small size features corresponding to the nanoelectrodes were cut all the way through. The cantilever's tip was also shortened down to about 2 μm in height (Figure 1C). This allowed one to reduce the mask-to-substrate distance and therefore increased the sharpness of the edges of the fabricated structures. For tip shortening, the cantilever was turned sideways by 90°. The pyramidal shape of the Si tip, with its sharp edges, allows one to obtain a sharp tip using a single cut.

The alignment of the cantilever (3) relative to the collimation mask (2) is essential, as will be explained in the following. The cantilever is mounted ex situ at a small tilt angle, of 1−5°, dictated by the requirement of having a homogeneous mask-to-substrate gap over the patterned area. Additional angle adjustment is enabled by the home-built tilt alignment stage.[20] The cantilever is positioned relative to the collimation mask under an optical microscope in such a way that only its end (i.e., about 80−150 μm of its length) is exposed to the evaporator beam (see Figure 1A). There are several reasons for this: (i) It minimizes the bending (typically, less than 100 nm) of the cantilever caused by the material that also coats the cantilever during evaporation. This fact, combined with the cantilever being almost parallel to the substrate surface, results in a very small lateral positioning error. Hence, the precision of pattern positioning does not degrade during continued material deposition. (ii) The laser used for the lever deflection detection during AFM can now be focused on the nonexposed part of the cantilever, toward its basis. This has the great advantage that it allows one to avoid readjustment of the scanning parameters during complex nanofabrication/imaging sequences. (iii) It minimizes the absorbed thermal radiation and hence changes of the cantilever's oscillator parameters. (iv) It allows the stiffness of the cantilever to remain essentially constant after material evaporation. This fact then made possible the implementation of a procedure for precise in situ detection of the material evaporation rate, described below.

The electrical probes (4,5) are made out of AuPd alloy, with 50 μm thick palladium wires attached at the ends. These wires are about 4 mm long and bent to an L shape in order to be elastic in all directions. The probes are mounted on small manipulators, which are also part of the assembly (1). These manipulators allow the adjustment of the probes' positions individually under an optical microscope. The probes' lateral position has to be such so that they fit onto the large pads (see Figure 1D). The position perpendicular to the substrate plane is adjusted to be 100 μm in front of the cantilever's tip: this allows a certain amount of contact force to build up when the cantilever approaches the substrate. Static friction holds the probes in place on the pads, even if the lateral position of the coupled cantilever is changed by a small distance, such as during scanning. The probes can slide onto the contact pads only when the cantilever is being moved over larger distances ($\geq$10 μm). However, even in such a case, the contact resistance between the probes and the contact pads stabilizes to reproducible values after sliding has occurred.

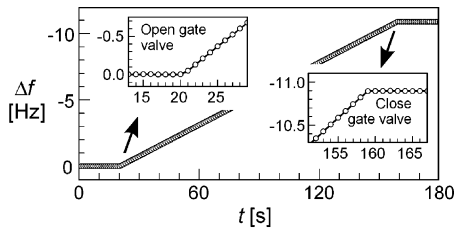

Figure 2. Shift of the cantilever resonance frequency as a function of the evaporation time (material: Pd). The insets magnify the variations at the start and stop of the evaporation. $\Delta f = -1$ Hz corresponds to 0.11 nm of Pd, as calibrated with AFM. The starting frequency was $f_0 = 27$ kHz.

For creating the micrometer-sized part of the electrodes, consisting of bonding pads and larger size connecting wires, a large-scale mask, similar to that in ref 20, was also produced using metallic foils. One actually starts the device by first using this large-scale mask to define the rectangular pads and a connecting line (10) on the substrate (9). The width of the pads is about 200 μm, which is large enough to accommodate in situ palladium probes (4,5) (ref 19) and also convenient for standard wire bonding for ex situ measurements. This large-scale pattern defines the overall size of the device, of about 0.9×0.7 mm^2; this is small enough to allow the fabrication of dozens of devices on the same substrate.

Because during evaporation material deposits simultaneously on the cantilever and the substrate, it is possible to estimate the thickness of the deposited electrodes from the changes in the cantilever's resonance frequency, f_r. Cantilevers have been used for various detection applications,[27,28] including mass detection of adsorbed metals. As only the end of the cantilever (about 25% of its length) is exposed to the evaporation beam, the f_r change is almost entirely caused by the additional deposited mass and much less by the change in the cantilever's stiffness, as mentioned above. Figure 2 shows f_r decreasing smoothly while the film thickness increases. Because the stiffness of the cantilever is not precisely known, the relation between frequency change and film thickness has to be calibrated, for example, using AFM. Once this is done, the evaporation rate for all materials can be calculated from their mass density. Apart from the decrease of f_r, we did not observe any changes in the other mechanical properties of the cantilever due to the deposited material.

All these technical implementations allowed us to also achieve the best merit figure for lateral positioning using dynamic nanostenciling. This is demonstrated on asymmetric, Pd−Ti nanogap structures realized on an insulating substrate (Figure 3). We could reproducibly achieve gaps as small as

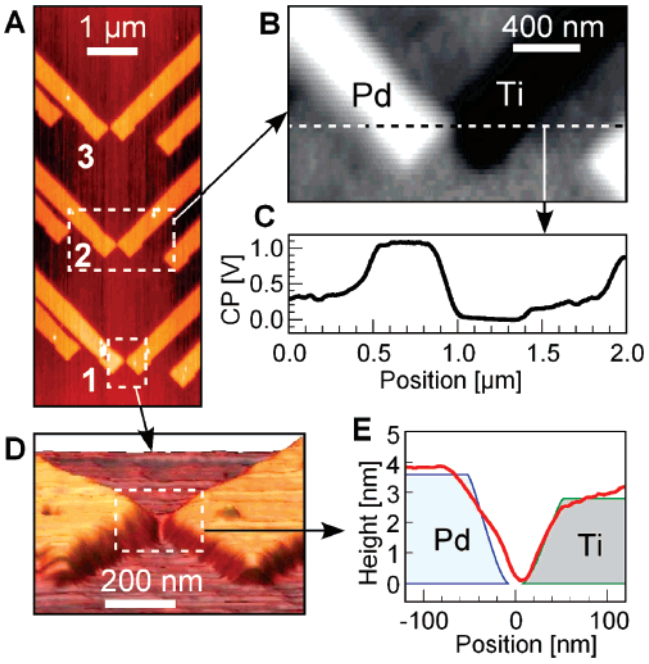

Figure 3. Asymmetric gap structures (left: Pd; right: Ti; thickness: 3−4 nm; substrate: SiO_2/Si). (A) Ex situ tapping mode image of three gap structures fabricated with different gap widths w ($w_1 > w_3 > w_2$; these values were programmed to each differ by 15 nm). Intergap resistances were measured in situ using the AFM tip (on the Pd electrodes) and one of the microprobes (connected to the Ti electrodes). The resistance values correlate with the gap size: $R_1 = 8$ TΩ; $R_3 = 0.5$ GΩ; $R_2 < 1$ MΩ (applied voltage: 1 V). (B) In situ Kelvin probe microscopy (KPM) image of structure 2. (C) Contact potential (CP) single line scan corresponding to the dotted line in (B). (D) Ex situ AFM image of structure 1 in tapping mode. (E) Line scan profile measured over the center of the nanogap from (D) (in red) and expected wedge thickness profile (blue/green) calculated using the shadow effect of the mask-cantilever and neglecting diffusion. For Ti, the electrode edge matches well with the expected profile, whereas for Pd, the edge is about 40 nm wider than expected due to diffusion.

20 nm (see Supporting Information for gap size estimation), such as for gap structure (1) from Figure 3, with very good electrical insulation (intergap resistance of about 8 TΩ) on the bare substrate. There is some material-dependent diffusion, as seen in Figure 3E (see Supporting Information for a discussion). Here we compare the experimental edge profiles of the Pd and Ti electrodes with their corresponding profiles calculated assuming zero diffusion. Accordingly, the experimental edge of the Pd electrode is widened by about 40 nm and is also wider than both the experimental and calculated edges of the Ti electrode by a few tens of nanometers. The difference between the experimental and calculated profiles for the Ti electrodes is much smaller, showing that in this case diffusion effects for Ti are less important than for Pd. Together with the high resistance of the 20 nm gap, it follows that our technique does not produce conductive paths on a scale down to a few tens of nm. This means that nanostenciling compares very favorably with beam-induced electrode deposition techniques, where leakage currents were recorded over the micrometer range.[8]

Figure 4A shows SWCNTs dispersed on an atomically flat sapphire substrate. To fabricate interconnects on them,

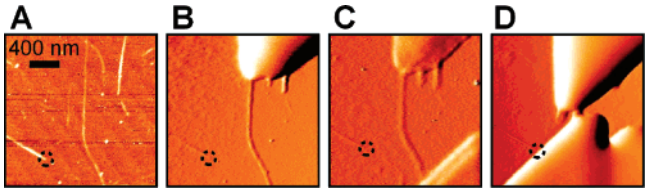

Figure 4. Connecting an individual SWCNT. (A) Noncontact AFM image of SWCNTs dispersed on a sapphire substrate with atomically flat terraces. (B) Topographic image after fabrication of the first electrode, (C) after adding the second electrode, and (D) after gap reduction to about 100 nm. Electrode material: Ti (7 nm thick). (B−D) are derivatives of topography. A dotted circle marks the end of the same nanotube used as a marker. The mask-cantilever used had the tip at original size, leading to a mask-to-substrate distance of about 15 μm.

we followed a general protocol: (i) large pads deposition (usually 5 nm of Ti followed by 50 nm of Au), (ii) AFM location of an appropriate nanotube or nanostructure (an area of about 30 × 50 μm^2 is available for searching, as masked by the cantilever's body and seen in Figure 1E), (iii) fabrication of the first nanoelectrode on the nanotube, (iv) fabrication of a nanoelectrode on the bare substrate, 100 nm away from the nanotube to check for the absence of surface leakage current, and (v) fabrication of the second electrode contacting the nanotube, with simultaneous in situ monitoring of the conduction established through the nanotube using the two wire probes. During structure fabrication, the cantilever's tip is retreated by 150 nm.

Parts B−D of Figure 4 show noncontact AFM (nc-AFM) images at various stages during this fabrication process over an individual SWCNT. They were recorded with the same cantilever used for fabrication after the deposition of the first Ti nanoelectrode, after the deposition of the second Ti nanoelectrode, and after reducing the gap between the electrodes down to about 100 nm, respectively. Gap reduction is a powerful way to elucidate transport mechanisms through 1D nanostructures.[29] For the nanostencil, this capability is built-in. Reproducible, insulating 20 nm gaps were demonstrated in Figure 3. This gap figure indicates the minimum size of structures that can be reliably connected currently, while work is in progress to decrease this figure further.

Figure 5 shows a SWCNT connected with Pd electrodes[30] according to the procedure above and then electrically characterized. In-situ $I-V$ curves were measured between electrodes at all stages using the two-wire Pd probes described previously. This allowed us to determine that the second electrode becomes continuous and fully operational after 4 nm of Pd film deposition. Pd electrodes were chosen, as they have been shown to greatly minimize the Schottky barriers that usually form at the SWCNT/metal interface.[30] The resulting dual terminal $I-V$ curve is ohmic, with a total resistance of 192 kΩ, while the Pd/nanotube contact resistance is less than 10 kΩ, as reported in literature.[31] To understand the origin of the resistance along the nanotube, we used the conductive (Cr coated) AFM tip as a third electrode to perform potentiometry measurements along the contacted nanotube. The potential was measured at specific points, as indicated in Figure 5B. The conductance per length

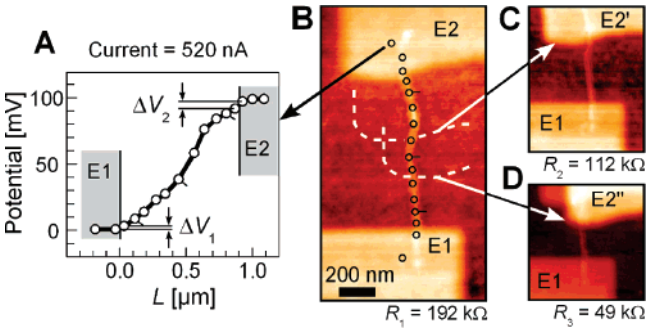

Figure 5. Two-probe electrical characterization and potentiometry on a SWCNT device on sapphire. (A) Potentiometry, with measurements taken at the points marked with circles in (B). Electrode E2 was biased with 100 mV, while E1 was grounded. The potential along the tube shows regions with different slopes, indicating inhomogeneous electrical properties of the tube. The current through the SWCNT was 520 nA, which corresponds to a total resistance of $R_0 = 192$ kΩ. The upper limits of the contact resistances, estimated from the voltage differences near the electrodes $\Delta V_{1,2}$, are $R_{E1} < 4.8$ kΩ, $R_{E2} < 10.4$ kΩ. "Moving" the electrode E2 as in (C) and (D) to reduce the interelectrode gap led to resistance reduction. In (D), only the homogeneous part of the nanotube bridges the electrodes. The technique thus allows one to select an arbitrary part of a larger nanostructure for studying. The thickness of the Pd electrodes is 4.5 nm (E1, E2, E2′) and 7 nm (E2″), respectively.

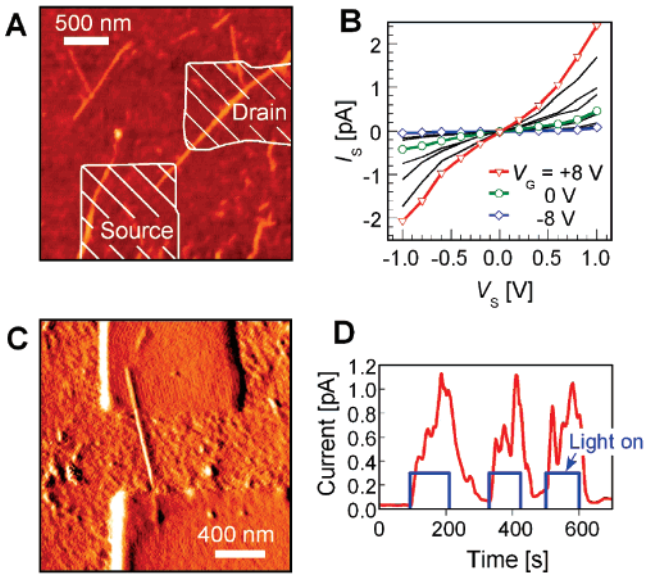

Figure 6. Porphyrin J-aggregate devices (substrate: SiO_2 (100 nm)/Si). (A,B) Gate-dependent current through a porphyrin J-aggregate bundle. (A) Nc-AFM image recorded before the fabrication of the electrodes. A part of a relatively large, inhomogeneous structure was connected. (B) In situ FET-type measurements at different gate voltages show a strong conductance increase at positive gate voltages. (C,D) Photoconductivity of a connected individual porphyrin J-aggregate. (C) In situ nc-AFM image of the device structure (derivative of topography). (D) Current variation through the device during on/off switching of the light source (applied voltage = 1 V; light source: $\lambda = 488$ nm, intensity ≈ 20 kW/m^2; measured ex situ in argon atmosphere). The thickness of the Pd electrodes is 5 nm.

(i.e., the slope of the curve in Figure 5A) shows clear variations: the middle part is significantly less conductive than the regions closer to the electrodes. This is consistent with the morphology of the tube (Figure 5B), which shows a small distorted middle section, usually associated with a defective region of increased resistivity.[32] The overall potentiometry curve is characteristic of a semiconducting nanotube with small contact resistance. Parts C and D of Figure 5 show the gap between the electrodes being reduced (as shown schematically in Figure 5B) so that a specific part of the nanotube is selected and probed. The corresponding resistance decreased each time, as expected, and in agreement with the measurements from Figure 5A.

We also used porphyrin J-aggregates as an example of "soft" nanostructures. These are supramolecular nanomaterials formed by hierarchical self-assembly of porphyrin *meso*-tetrakis(4-sulfonatophenyl)porphine (TPPS4) molecules[17,18] first into intermediate linear structures, which assemble further into a more complex structure, of about 4 nm in height when flattened by a supporting surface.[17,18,33] Such J-aggregates can then also form bundles. Parts A and C of Figure 6 show interconnection of a small bundle and an individual J-aggregate, respectively, on SiO_2/Si substrate, used for further electro-optical characterization. The same general nanofabrication protocol described above was employed. For the device in Figure 6A, three terminal, FET-type with back gate, measurements were performed. The source−drain current is small (in or below the pA range) at all gate voltages, as extrapolated from published measurements,[34] where thousand of such molecular aggregates and bundles were contacted between the probing electrodes. Such low current values reflect the molecular nature of the nanostructure. There is good gate voltage control (Figure 6B), with large negative voltages quenching the conduction, while a positive gate voltage increases the source−drain current. This is consistent with transport through overlapping LUMOS of individual molecules or groups of molecules that form the supramolecular structure.[34] Parts C and D of Figure 6 give a further proof that the fabricated devices are fully functional: expected photoconductivity[34] was clearly detected in an individual J-aggregate under light of 488 nm wavelength, appropriate to excite HOMO−LUMO transitions. Figure 6D shows the response of the nanostructure under on/off switching of the laser. Note that the bundle from Figure 6A did not show photoconductivity though conductive, highlighting the need to individually investigate such structures and not as an ensemble of them as done in previous works.[34] We believe that these are the first such measurements performed on individual porphyrin J-aggregates or a small bundle thereof.

In conclusion, we demonstrated a method for prototype fabrication/characterization based on dynamic nanostenciling, which allows the integration of chosen, individual preexisting nanostructures into devices using entirely scanning probe based methods and without exposure to damaging conditions, such as high-energy charged particles, heat, or resists.

Dynamic nanostenciling is not a maskless technique, like ion and electron beam-assisted deposition, but relevant patterning problems can be solved by using a "standard mask" designed for a rather general situation, while the

precise device geometry is defined through the flexibility of the mask positioning. The masks can therefore be batch-fabricated, e.g., by parallel lithography techniques,[35] instead of FIB, a serial technique used here for convenience.

We showed that devices integrating nanostructures could be fabricated using not very fine mask apertures, of a few hundred of nm in width, by taking advantage of the nanoscale positioning accuracy of the instrument. Therefore, very small (tens of nm or below) mask apertures, subjected to a serious clogging problem,[15,36] were not required. Currently, we can fabricate structures relative to any pre-existing object with a precision of 20 nm. This is already sufficient for many applications. Further improvement in positioning accuracy is possible by rigorously choosing materials with matching thermal expansion coefficients or higher thermal conductance coefficients, by fabricating the apertures closer to the tip, and by analyzing and compensating the constant drift components. With the technical components developed here, a failure of the fine mask, i.e., due to clogging or stress-induced deformation,[36] never occurred. The technique requires dedicated equipment, but the operation strategy described is relatively "user-friendly". These facts may help convince that dynamic nanostenciling is a practical technique that could be applied in a routine way.

Carbon nanotubes and porphyrin supramolecular aggregates were used as examples of integrated nanostructures, but the technique can be applied to a large range of nanomaterials, including those that are unprocessable by standard, beam-assisted techniques.

Acknowledgment. We thank Professor Ricardas Rotomskis for providing us the porphyrin J-aggregates. This work was funded through the Special Coordination Funds for Promoting Science and Technology from the Ministry of Education, Culture, Sports, Science, and Technology of the Japanese Government. This work was partially supported by the International Cooperative Research Project (ICORP) of the Japan Science and Technology Agency.

Supporting Information Available: Experimental methods for sample preparation and characterization techniques; procedure for estimation of gap sizes; discussion of diffusion; and estimation of temperature change caused by evaporator are provided. This material is available free of charge via the Internet at http://pubs.acs.org.

References

(1) Geim, A. K.; Novoselov, K. S. *Nat. Mater.* **2007**, *6*, 183−191.
(2) Meyer, R. R.; Sloan, J.; Dunin-Borkowski, R. E.; Kirkland, A. I.; Novotny, M. C.; Bailey, S. R.; Hutchison, J. L.; Green, M. L. H. *Science* **2000**, *289*, 1324−1326.
(3) Li, Y.; Qian, F.; Xiang, J.; Lieber, C. M. *Mater. Today* **2006**, *9*, 18−27.
(4) Zhang, S. G. *Nat. Biotechnol.* **2003**, *21*, 1171−1178.
(5) Katz, E.; Willner, I. *ChemPhysChem* **2004**, *5*, 1085−1104.
(6) Nabity, J.; Campbell, L. A.; Zhu, M.; Zhou, W. E-Beam Nanolithography Integrated with Scanning Electron Microscope. In *Scanning Microscopy for Nanotechnology*; Zhou, W., Wang, Z. L., Eds.; Springer: Berlin, 2007; pp 120−151.
(7) Langford, R. M. *J. Nanosci. Nanotechnol.* **2006**, *6*, 661−668.
(8) Gopal, V.; Radmilovic, V. R.; Daraio, C.; Jin, S.; Yang, P. D.; Stach, E. A. *Nano Lett.* **2004**, *4*, 2059−2063.
(9) Randolph, S. J.; Fowlkes, J. D.; Rack, P. D. *Crit. Rev. Solid State Mater. Sci.* **2006**, *31*, 55−89.
(10) Cholet, S.; Joachim, C.; Martinez, J. P.; Rousset, B. *Eur. Phys. J.: Appl. Phys.* **1999**, *8*, 139−145.
(11) Egger, R.; Bachtold, A.; Fuhrer, M. S.; Bockrath, M.; Cobden, D. H.; McEuen, P. L. Luttinger liquid behavior in metallic carbon nanotubes. In *Interacting Electrons in Nanostructures*, Haug, R., Schoeller, H., Eds.; Springer: Berlin, 2001; p 125.
(12) Bezryadin, A.; Verschueren, A. R. M.; Tans, S. J.; Dekker, C. *Phys. Rev. Lett.* **1998**, *80*, 4036−4039.
(13) Zhou, Y. X.; Johnson, A. T.; Hone, J.; Smith, W. F. *Nano Lett.* **2003**, *3*, 1371−1374.
(14) Ono, K.; Shimada, H.; Kobayashi, S. I.; Ootuka, Y. *Jpn. J. Appl. Phys., Part 1* **1996**, *35*, 2369−2371.
(15) Deshmukh, M. M.; Ralph, D. C.; Thomas, M.; Silcox, J. *Appl. Phys. Lett.* **1999**, *75*, 1631−1633.
(16) Luthi, R.; Schlittler, R. R.; Brugger, J.; Vettiger, P.; Welland, M. E.; Gimzewski, J. K. *Appl. Phys. Lett.* **1999**, *75*, 1314−1316.
(17) Schwab, A. D.; Smith, D. E.; Rich, C. S.; Young, E. R.; Smith, W. F.; de Paula, J. C. *J. Phys. Chem. B* **2003**, *107*, 11339−11345.
(18) Rotomskis, R.; Augulis, R.; Snitka, V.; Valiokas, R.; Liedberg, B. *J. Phys. Chem. B* **2004**, *108*, 2833−2838.
(19) Egger, S.; Higuchi, S.; Nakayama, T. *J. Comb. Chem.* **2006**, *8*, 275−279.
(20) Egger, S.; Ilie, A.; Fu, Y. T.; Chongsathien, J.; Kang, D. J.; Welland, M. E. *Nano Lett.* **2005**, *5*, 15−20.
(21) Gross, L.; Schlittler, R. R.; Meyer, G.; Vanhaverbeke, A.; Allenspach, R. *Appl. Phys. Lett.* **2007**, *90*, 093121.
(22) Zahl, P.; Bammerlin, M.; Meyer, G.; Schlittler, R. R. *Rev. Sci. Instrum.* **2005**, *76*, 023707.
(23) Cojocaru, C. V.; Harnagea, C.; Rosei, F.; Pignolet, A.; van den Boogaart, M. A. F.; Brugger, J. *Appl. Phys. Lett.* **2005**, *86*, 183107.
(24) Guo, H. M.; Martrou, D.; Zambelli, T.; Polesel-Maris, J.; Piednoir, A.; Dujardin, E.; Gauthier, S.; van den Boogaart, M. A. F.; Doeswijk, L. M.; Brugger, J. *Appl. Phys. Lett.* **2007**, *90*, 093113.
(25) Persaud, A.; Park, S. J.; Liddle, J. A.; Schenkel, T.; Bokor, J.; Rangelow, I. W. *Nano Lett.* **2005**, *5*, 1087−1091.
(26) Mutzel, M.; Muller, M.; Haubrich, D.; Rasbach, U.; Meschede, D.; O'Dwyer, C.; Gay, G.; De Lesegno, B. V.; Weiner, J.; Ludolph, K.; Georgiev, G.; Oesterschulze, E. *Appl. Phys. B: -Lasers Opt.* **2005**, *80*, 941−944.
(27) Lavrik, N. V.; Sepaniak, M. J.; Datskos, P. G. *Rev. Sci. Instrum.* **2004**, *75*, 2229−2253.
(28) Thundat, T.; Oden, P. I.; Warmack, R. J. *Microscale Thermophys. Eng.* **1997**, *1*, 185−199.
(29) Buttiker, M.; Imry, Y.; Landauer, R.; Pinhas, S. *Phys. Rev. B* **1985**, *31*, 6207−6215.
(30) Javey, A.; Guo, J.; Wang, Q.; Lundstrom, M.; Dai, H. J. *Nature* **2003**, *424*, 654−657.
(31) Mann, D.; Javey, A.; Kong, J.; Wang, Q.; Dai, H. J. *Nano Lett.* **2003**, *3*, 1541−1544.
(32) Bachtold, A.; Fuhrer, M. S.; Plyasunov, S.; Forero, M.; Anderson, E. H.; Zettl, A.; McEuen, P. L. *Phys. Rev. Lett.* **2000**, *84*, 6082−6085.
(33) Kitahama, Y.; Kimura, Y.; Takazawa, K. *Langmuir* **2006**, *22*, 7600−7604.
(34) Schwab, A. D.; Smith, D. E.; Bond-Watts, B.; Johnston, D. E.; Hone, J.; Johnson, A. T.; de Paula, J. C.; Smith, W. F. *Nano Lett.* **2004**, *4*, 1261−1265.
(35) van den Boogaart, M. A. F.; Kim, G. M.; Pellens, R.; van den Heuvel, J. P.; Brugger, J. *J. Vac. Sci. Technol. B* **2004**, *22*, 3174−3177.
(36) Lishchynska, M.; Bourenkov, V.; van den Boogaart, M. A. F.; Doeswijk, L.; Brugger, J.; Greer, J. C. *Microelectron. Eng.* **2007**, *84*, 42−53.

NL071778M